

Sparse convolutional context-aware multiple instance learning for whole slide image classification

Marvin Lrousseau^{1,2}, Maria Vakalopoulou¹, Nikos Paragios³, and Eric Deutsch²

¹ Paris-Saclay University, CentraleSupélec, 91190, Gif-sur-Yvette, France

² Paris-Saclay University, Gustave Roussy, Inserm, 94800, Villejuif, France

³ TheraPanacea, 75014, Paris, France

Abstract. Whole slide microscopic slides display many cues about the underlying tissue guiding diagnostic and the choice of therapy for many diseases. However, their enormous size often in gigapixels hampers the use of traditional neural network architectures. To tackle this issue, multiple instance learning (MIL) classifies bags of patches instead of whole slide images. Most MIL strategies consider that patches are independent and identically distributed. Our approach presents a paradigm shift through the integration of spatial information of patches with a sparse-input convolutional-based MIL strategy. The formulated framework is generic, flexible, scalable and is the first to introduce contextual dependencies between decisions taken at the patch level. It achieved state-of-the-art performance in pan-cancer subtype classification. The code of this work will be made available at *censored for review*.

Keywords: Multiple instance learning · Whole slide image classification · Weakly supervised learning.

1 Introduction

Histopathology, or the microscopic examination of tissues, is essential in diagnostic medicine. The advent of digital scanners is leading to an increasing digitization of microscopic slides into whole slide images (WSI) [22]. These images encompass a great deal of information about the phenotypes of cells and reach billions of pixels, preventing the use of traditional convolutional neural networks (CNN) due to memory limitations. Downscaling is not viable since most of the cues about a tumor are displayed at the cell-level (or nuclei-level), which are lost with downsampling. Besides, WSI cannot be classified from a contiguous extracted region since pertinent information may not be evenly spread in those images due to tumor heterogeneity [12]. Therefore, the scientific community has predominantly adopted the strategy of classifying patches extracted throughout WSI using the multiple instance learning [9] paradigm.

In this work, we propose a novel type of framework built on top of multiple instance learning that exploits the spatial structure of WSI with the use of sparse-input convolutional neural networks. In particular, our methodology is designed

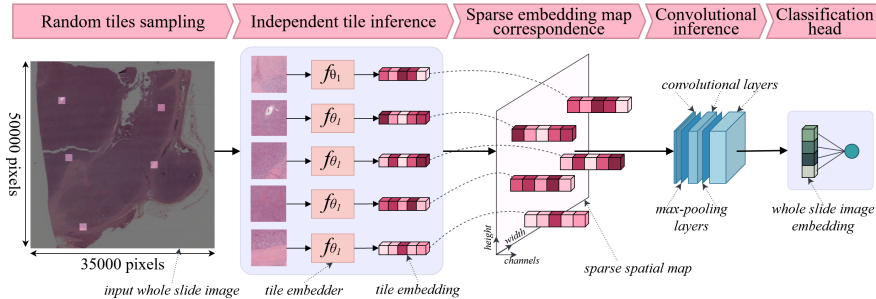


Fig. 1: Visual representation of the proposed approach. First, a set of patches are randomly sampled throughout a WSI, and are then concurrently and independently forwarded into a shared patch embedder f_{θ_1} . Then, a sparse map is built by placing each resulting embedding at the location of its associated patch. This map is forwarded into a sparse-input CNN producing a bag embedding which is finally classified into probabilities.

to harvest the spatial context of patches as additional information for improving WSI classification. On another hand, the relative localization of patches should enhance the consistency of features from neighboring patches which often display the same tissue phenotypes. Our contributions are twofold: (i) we propose a novel sparse embedding map to fully process huge WSI keeping the spatial relations of the different instances, (ii) large scale experiments with other state of the art MIL schemes prove the high potentials of our formulation. Our framework is open-sourced at *censored for review*.

2 Background

2.1 Multiple instance learning

MIL deals with problems where labels are associated with groups of instances, or bags (whole slide images in our case), whereas instance (tiles or patches) labels are unknown or non-existent. In the most general case, MIL models can be decomposed into 3 parts: an instance embedder f_{θ_1} , a pooling operator g_{θ_2} and a classifier h_{θ_3} such that a prediction for a bag (x_1, \dots, x_K) is obtained with $h_{\theta_3}(g_{\theta_2}(f_{\theta_1}(x_1), \dots, f_{\theta_1}(x_K)))$. Instance-level MIL is a particular case of MIL where embeddings are one-dimensional *i.e.* apparent to probabilities. Most of the MIL community efforts have revolved around the pooling operator g_{θ_2} which can be placed in two categories: permutation invariant operators, and others.

Permutation invariant pooling operators In some applications, such as the drug discovery problem [3], instances do not exhibit dependency, ordering, or spatial information among each other, *i.e.* they are independent and identically distributed (i.i.d.). Equivalently, for any permutation σ , the output of an i.i.d.

pooling operator is the same for (x_1, \dots, x_K) and $(\sigma(x_1), \dots, \sigma(x_K))$, *i.e.* they are permutation invariant, such as:

$$\begin{aligned}
 \text{mean} & : (x_1, \dots, x_K) \mapsto \frac{(x_1 + \dots + x_K)}{K} \\
 \text{max} & : (x_1, \dots, x_K) \mapsto \max(x_1, \dots, x_K) \\
 \text{log-sum-exp [13]} & : (x_1, \dots, x_K) \mapsto \frac{1}{M} \log \left(\sum \exp(M \times x_k) \right) \\
 \text{attention [8]} & : (x_1, \dots, x_K) \mapsto \sum_k \frac{\exp(w^\top \tanh(Vx_k^\top))}{\sum_k \exp(w^\top \tanh(Vx_j^\top))} \cdot x_k \\
 \text{gated-attention [8]} & : (x_1, \dots, x_K) \mapsto \sum_k \frac{\exp(w^\top (\tanh(Vx_k^\top) \odot \text{sigm}(Ux_k^\top)))}{\sum_k \exp(w^\top (\tanh(Vx_j^\top) \odot \text{sigm}(Ux_j^\top))} \cdot x_k
 \end{aligned}$$

where $M \in \mathbb{R}^+$, $V \in \mathbb{R}^{L \times \dim(\mathbb{H})}$, $U \in \mathbb{R}^{L \times \dim(\mathbb{H})}$, $w \in \mathbb{R}^{L \times 1}$, $L \in \mathbb{N}^*$ are parameters, \odot is the elementwise multiplication, and sigm is the elementwise sigmoid function.

Permutation noninvariant pooling operators The i.i.d. assumption does not hold for applications where there is inherent structural information about instances, such as document classification from sentences [1], or WSI classification from tiles. Zhou et al. [24] have notably achieved state-of-the-art performance over i.i.d. MIL poolings by building a graph from instance embeddings, and then performing classification with kernel methods. With recent improvements of graph neural networks [20], further iterations have been proposed by the community [18,21,23].

2.2 Sparse-input convolutional neural network

Convolutional layers are optimized for dense inputs such as natural images or 3D medical volumes but are not efficient for sparse data in terms of both memory consumption and FLOPs. Sparse data can be defined as variables containing few *active* cells, *i.e.* most of their volume is *empty* - examples are cloud points from LiDAR or tiles extracted from WSI. In particular and for clarity, the sparsity in sparse-input CNN is related to the input, and not to the weights sparsity which is another matter. Several convolutional implementations designed for sparse input data have been proposed [4,5,14,6] revolving around the idea that convolutions should only be performed on *active* data points, *i.e.* by ignoring empty input regions, therefore decreasing the number of computations. Additionally, sparse data have their own tensor structure which considers only *active* data points, therefore using virtually no memory for non-*active* tensor cells.

3 Methods

We propose to use a sparse-input convolutional neural network to learn the MIL operator in whole slide image classification applications; we coin our framework

SparseConvMIL (Figure 1). More specifically, our pooling operator first builds a sparse map of instance embeddings, which is then processed into a bag embedding with a sparse-CNN.

Let us consider one input WSI $X \in [0, 1]^{w \times h \times 3}$, where w and h are typically in dozens of thousands. b locations $l_X = (i_k, j_k)$ are randomly sampled from X . A tile (x_{i_k, j_k}) is extracted from each location. Providing an instance embedder f_{θ_1} , all tiles are independently and concurrently inferred, producing the set of b embeddings $f_{\theta_1}(x_{i_k, j_k}) \in \mathbb{H}$. The sparse embedding map S^X is built by corresponding each tile embedding with their location:

$$S^X = \left\{ [(i_k, j_k), f_{\theta_1}(x_{i_k, j_k})]; 1 \leq k \leq b \right\} \subset (\mathbb{N} \times \mathbb{N} \times \mathbb{H})^b$$

Alternatively, S^X can be characterized by:

$$\forall i \in \llbracket 1, w \rrbracket, \forall j \in \llbracket 1, h \rrbracket : S_{i,j}^X = \begin{cases} \emptyset & \text{if } (i, j) \notin l_X \\ f_{\theta_1}(x_{i,j}) & \text{otherwise} \end{cases}$$

Once S^X is reconstructed, it is forwarded into a sparse-input CNN which can be made of convolutional layers, pooling layers, and global pooling layers. For a convolution layer $U \in \mathbb{R}^{2f+1} \times \mathbb{R}^{2f+1} \times \mathbb{R}^o$ with a filter of half-size f , stride s , and o output channels, the output $U \circledast S^X$ is:

$$\forall i \in \llbracket 1, \lfloor \frac{w}{s} \rfloor \rrbracket, \forall j \in \llbracket 1, \lfloor \frac{h}{s} \rfloor \rrbracket : (U \circledast S^X)_{i,j} = \sum_{m=-f}^f \sum_{n=-f}^f U_{m+f, n+f} \cdot S_{si+m, sj+n}^X$$

where a term $S_{si+m, sj+n}^X = \emptyset$ has no impact in the sum. In particular, for a position (i, j) , if no embeddings are present in a neighboring region of half-width f , *i.e.* when the set $\{S_{X;m,n}; |m-i| \leq f, |n-j| \leq f\}$ is empty, the output of the convolution is \emptyset which implies that the output $U \circledast S^X$ is also sparse.

Similarly, for a function p such as the functions max or average, a pooling layer with filter size f and stride s produces the output $p(S^X)$ from an input sparse map S^X such that:

$$\forall i \in \llbracket 1, \lfloor \frac{w}{s} \rfloor \rrbracket, \forall j \in \llbracket 1, \lfloor \frac{h}{s} \rfloor \rrbracket : p(S^X)_{i,j} = p(\{S_{si+m, sj+n}^X; m \leq f, n \leq f\})$$

In particular, adaptive global pooling layers with output size o are defined as pooling layers of stride 1 and of filter size $\lfloor \frac{w}{o} \rfloor$ and $\lfloor \frac{h}{o} \rfloor$. Noteworthy, locations with no data do not interfere with the pooling function.

Eventually, after a succession of sparse-input layers, a bag embedding is obtained. Bag probabilities are then computed with any type of classifier, including multi-layer perceptrons.

We introduce an additional parameter called the *downsampling* factor. In theory, a sparse map thus built has the same size as its associated WSI. However in practice, few tiles can be extracted from a WSI, implying that most convolutional operations would involve at most one activate size which would

cancel out the effect of convolutions. To address this issue, sparse maps can be downsampled, *i.e.* all tile locations can be divided by a shared factor - the *downsampling* factor. We evaluate its impact in our experiments.

Finally, SparseConvMIL benefits from additional data augmentation over permutation noninvariant pooling strategies, precisely because it treats instances as non i.i.d. Spatial augmentations (*e.g.* flipping, rotations, local shuffling or elastic deformations) performed on tiles locations, or equivalently on the sparse map, can help reduce the burden of overfitting by increasing the input data to the pooling CNN. Besides, these augmentations can be performed after tile embedding inference, implying that multiple sparse map spatial augmentations can be done with a low additional memory footprint.

4 Experimental validation

We have used two well studied data examples to demonstrate the extreme potentials of our method. The first is CRCHISTOPHENOTYPE for classifying whether power fields contain epithelial cells, and the second is THE CANCER GENOME ATLAS for pan-cancer subtype classification.

4.1 Classical MIL dataset

Dataset The CRCHISTOPHENOTYPE [17] dataset consists of 100 haematoxylin and eosin-stained (H&E) 500×500 pixels histology images of colorectal adenocarcinomas. A total of 22,444 nuclei were annotated with the position of their center and their type amid epithelial, inflammatory, fibroblast, or miscellaneous. In this context, bags are made of 27×27 pixel patches extracted around each nuclei center, and are considered positive iff they contain at least one epithelial cell, resulting in 51 positive and 49 negative bags.

Implementation details All methods share the same training parameters which are detailed thereafter. The instance embedding model f_{θ_1} (supplementary data Table 1) proposed in [17] and used in [8] is employed. Binary cross-entropy computes error signals which update the models parameters using Adam optimizer [10] with default momentum values, learning rate of $1e^{-4}$, weight decay of $5e^{-4}$, batch size of 1 for 100 epochs. For data augmentation, tiles are randomly rotated and flipped. Besides, each tile is first color deconvoluted in the HE space using [15], then reconstructed into RGB space after multiplication of both H and E stains with two independent random gaussian variables with mean 1 and standard deviation of 3. Finally each tile is standard scaled with mean and standard deviation extracted from the training set. Sparse maps of the proposed approach are downsampled by 2, *i.e.* there are of width 250 pixels. All methods share the same data split with 55, 20 and 25 samples for resp. the training, validation and testing sets. The validation set is used to select the snapshot with least validation error for inference on the testing set.

Attention-based approaches use a two-layer neural network for attention with 128 hidden neurons as used in [8], resulting in 66304 pooling parameters and 131968 for the gated version. The proposed SparseConvMIL is implemented with two 12-channels convolutional filters with filter size 3, resulting in a module with 56628 parameters, or less than both previous. The implementation of other methods are detailed in supplementary Table 2. The training/testing process was performed 5 times for each method to derive confidence intervals.

METHOD	ACCURACY	PRECISION	RECALL	F1-SCORE	AUC
Instance+max	0.842±0.021	0.866±0.017	0.816±0.031	0.839±0.023	0.914±0.010
Instance+mean	0.772±0.012	0.821±0.011	0.710±0.031	0.759±0.017	0.866±0.008
max	0.824±0.015	0.884±0.014	0.753±0.020	0.813±0.017	0.918±0.010
mean	0.860±0.014	0.911±0.011	0.804±0.027	0.853±0.016	0.940±0.010
Attention [8]	0.904±0.011	0.953 ±0.014	0.855±0.017	0.901±0.011	0.968 ±0.009
Gated-Attention [8]	0.898±0.020	0.944±0.016	0.851±0.035	0.893±0.022	0.968 ±0.010
Proposed	0.944 ±0.019	0.929±0.021	0.944 ±0.019	0.932 ±0.024	0.958±0.008

Table 1: Results on CRCHISTOPHENOTYPE in mean \pm standard deviation of 5 runs. Otherwise specified, methods are embedding-level MIL.

Results Results are reported in Table 1. The proposed approach achieves the best performance in terms of balanced accuracy and f1-score. Although the proposed obtained a slightly lower precision than the attention-based methods, it achieved a significantly higher recall. This is preferable for clinical practice since carcinomas arise from epithelial cells [19], which implies that no epithelial tissue should be discarded for exhaustive cancer screening.

4.2 Large-scale whole slide image dataset

Dataset 9,200 WSI were downloaded from THE CANCER GENOME ATLAS from all available solid cancer subtypes, resulting in 5.57Tb of data. These WSI were randomly selected among the slides with some neoplastic tissue, *i.e.* by not considering normal slides which provide no cue about a cancer subtype given their location since they have no tumor material. The number WSI per subtype and per location is reported in supplementary Table 3. All WSI were tiled into 512 pixels width tiles with 128 pixels overlap on both sides at 10 \times magnification using code from [11]. The cohort was split on a patient-basis in 3597, 2001 and 3602 slides for respectively training, validation and testing sets.

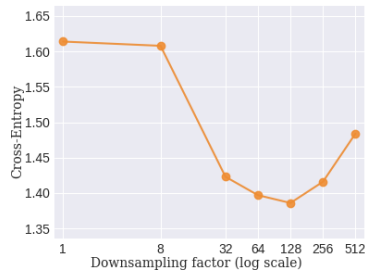
Implementation details All benchmarked methods use a ResNet34 architecture [7] pre-trained on Imagenet [2] as the instance embedding f_{θ_1} , and use one fully connected layer for classifier (mapping each bag embedding to a probability). For embedding-based methods, the last fully connected layer of ResNet34

was removed resulting in 512 output channels per tile instead of 1 probability. During training, 200 randomly cropped 128×128 pixel tiles were randomly sampled within each WSI. Data augmentation was the same as in the first experiment (subsection 4.1). Adam [10] was used with cross-entropy loss, learning rate of $1e^{-4}$ and batch size of 10 WSI (or 2000 taking into account the number of tiles per WSI). Due to significant imbalance in the class distribution, over-sampling was employed during training with frequencies equal to the inverse of the classes counts. For each method, the training process lasted approximately 1 week on 2 Nvidia V100. SparseConvMIL used two convolutional layers with varying numbers of channels. Downsampling was 128. Attention-based also used varying hidden neurons as specified.

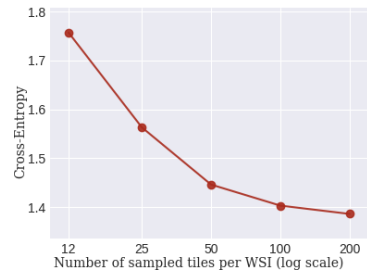
METHOD	#PARAMS	ACCURACY	PRECISION	F1-SCORE	AUC	CE
Random	N/A	0.031	0.031	0.031	0.500	3.506
Instance+max [†]	16k	0.417	0.365	0.360	0.879	2.027
Instance+mean [†]	16k	0.463	0.417	0.414	0.905	1.783
Instance+LSE [†]	16k	0.451	0.406	0.403	0.898	1.819
max [†]	70k	0.441	0.434	0.403	0.913	1.821
mean [†]	70k	0.488	0.463	0.456	0.917	1.604
Attention-128 [8]	82k	0.481	0.448	0.449	0.913	1.619
Attention-512 [8]	279k	0.487	0.451	0.453	0.912	1.616
Attention-2048 [8]	1055k	0.472	0.452	0.452	0.909	1.621
Gated-Attention-128 [8]	147k	0.492	0.452	0.456	0.916	1.613
Gated-Attention-512 [8]	542k	0.487	0.447	0.450	0.911	1.629
Gated-Attention-2048 [8]	2105k	0.483	0.457	0.459	0.911	1.604
Graph-CNN [18]	789k	0.464	0.439	0.436	0.907	1.673
Proposed-c32,c32	157k	0.523	0.508	0.504	0.935	1.386
Proposed-c128,c128	742k	0.568	0.568	0.553	0.944	1.267
Proposed-c256,c256	1772k	0.567	0.571	0.560	0.948	1.221

Table 2: Results of the 32 classes classification on the TCGA dataset. PARAMS are the number of pooling parameters (in thousand). ACCURACY is balanced. CE stands for cross-entropy. Random is the random performance. Otherwise specified, methods are embedding-level MIL. [†] denotes parameters-unscalable pooling methods.

Results Table 2 reports results for several metrics computed by averaging one-vs-all metrics for each class. The proposed approach achieved superior results in all metrics and for all configurations, even the small one with 32 channels convolutions. Furthermore, SparseConvMIL seemed to scale better than attention-based MIL. Indeed as inferred in Table 2, increasing the parameters of SparseConvMIL improved significantly performance. On the contrary, attention-based MIL stagnated with additional parameters.



(a) varying the downsampling factor



(b) varying the number of sampled tiles

Fig. 2: Performance of SparseConvMIL-c32,c32 by varying the input sparsity

We aimed at understanding the limitations of the proposed approach. Figure 2a plots the performance of SparseConvMIL-c32,c32 with various downsampling. In particular, the method performed significantly worse for low downsampling, which we conjecture is due to the fact that tiles are too far apart to exploit spatial context with convolution. Furthermore, its performance decreased for high downsamplings, *e.g.* 256 or 512, which is probably due to uncoalesced sparse maps, where there may be duplicate coordinates for several tiles provoking a loss of input tiles. Figure 2b plots the performance by varying the number of tiles sampled per WSI for downsampling of 128. The performance of SparseConvMIL increased with respect to the number of sampled tiles, which is not surprising since more tiles provide more information about WSI.

5 Conclusion

In this paper, we proposed a flexible and promising sparse-input convolutional MIL approach for classifying gigapixel images. We showed on one small-scale dataset that our method performs on par or better than other approaches for multiple metrics. We also demonstrated that the proposed approach achieves significant better performances for all metrics on very large-scale pan-cancer whole slide images classification from the public dataset The Cancer Genome Atlas. The limitations of our method have been measured with respect to the level of sparsity in input data.

There are several ways to iterate over this work. First, CNN visualization techniques, *e.g.* GradCAM [16], can be employed to decipher the key instances and improve interpretability of the framework. Besides, more sophisticated sparse-input CNN architectures could further improve performance, *e.g.* with more layers and residual connections [7].

References

1. Angelidis, S., Lapata, M.: Multiple instance learning networks for fine-grained sentiment analysis. *Transactions of the Association for Computational Linguistics* **6**, 17–31 (2018)
2. Deng, J., Dong, W., Socher, R., Li, L.J., Li, K., Fei-Fei, L.: Imagenet: A large-scale hierarchical image database. In: 2009 IEEE conference on computer vision and pattern recognition. pp. 248–255. Ieee (2009)
3. Dietterich, T.G., Lathrop, R.H., Lozano-Pérez, T.: Solving the multiple instance problem with axis-parallel rectangles. *Artificial intelligence* **89**(1-2), 31–71 (1997)
4. Engelcke, M., Rao, D., Wang, D.Z., Tong, C.H., Posner, I.: Vote3deep: Fast object detection in 3d point clouds using efficient convolutional neural networks. In: 2017 IEEE International Conference on Robotics and Automation (ICRA). pp. 1355–1361. IEEE (2017)
5. Graham, B.: Sparse 3d convolutional neural networks. arXiv preprint arXiv:1505.02890 (2015)
6. Graham, B., van der Maaten, L.: Submanifold sparse convolutional networks. arXiv preprint arXiv:1706.01307 (2017)
7. He, K., Zhang, X., Ren, S., Sun, J.: Identity mappings in deep residual networks. In: European conference on computer vision. pp. 630–645. Springer (2016)
8. Ilse, M., Tomczak, J., Welling, M.: Attention-based deep multiple instance learning. In: International conference on machine learning. pp. 2127–2136. PMLR (2018)
9. Keeler, J.D., Rumelhart, D.E., Leow, W.K.: Integrated segmentation and recognition of hand-printed numerals. *Microelectronics and Computer Technology Corporation* (1991)
10. Kingma, D.P., Ba, J.: Adam: A method for stochastic optimization. arXiv preprint arXiv:1412.6980 (2014)
11. Lerousseau, M., Vakalopoulou, M., Classe, M., Adam, J., Battistella, E., Carré, A., Estienne, T., Henry, T., Deutsch, E., Paragios, N.: Weakly supervised multiple instance learning histopathological tumor segmentation. In: International Conference on Medical Image Computing and Computer-Assisted Intervention. pp. 470–479. Springer (2020)
12. Marusyk, A., Polyak, K.: Tumor heterogeneity: causes and consequences. *Biochimica et Biophysica Acta (BBA)-Reviews on Cancer* **1805**(1), 105–117 (2010)
13. Ramon, J., De Raedt, L.: Multi instance neural networks. In: Proceedings of the ICML-2000 workshop on attribute-value and relational learning. pp. 53–60 (2000)
14. Riegler, G., Osman Ulusoy, A., Geiger, A.: Octnet: Learning deep 3d representations at high resolutions. In: Proceedings of the IEEE conference on computer vision and pattern recognition. pp. 3577–3586 (2017)
15. Ruifrok, A.C., Johnston, D.A., et al.: Quantification of histochemical staining by color deconvolution. *Analytical and quantitative cytology and histology* **23**(4), 291–299 (2001)
16. Selvaraju, R.R., Cogswell, M., Das, A., Vedantam, R., Parikh, D., Batra, D.: Grad-cam: Visual explanations from deep networks via gradient-based localization. In: Proceedings of the IEEE international conference on computer vision. pp. 618–626 (2017)
17. Sirinukunwattana, K., Raza, S.E.A., Tsang, Y.W., Snead, D.R., Cree, I.A., Rajpoot, N.M.: Locality sensitive deep learning for detection and classification of nuclei in routine colon cancer histology images. *IEEE transactions on medical imaging* **35**(5), 1196–1206 (2016)

18. Tu, M., Huang, J., He, X., Zhou, B.: Multiple instance learning with graph neural networks. arXiv preprint arXiv:1906.04881 (2019)
19. Warburg, O.: The metabolism of carcinoma cells. *The Journal of Cancer Research* **9**(1), 148–163 (1925)
20. Wu, Z., Pan, S., Chen, F., Long, G., Zhang, C., Philip, S.Y.: A comprehensive survey on graph neural networks. *IEEE transactions on neural networks and learning systems* (2020)
21. Yi, Y., Lin, M.: Human action recognition with graph-based multiple-instance learning. *Pattern Recognition* **53**, 148–162 (2016)
22. Zarella, M.D., Bowman, D., Aeffner, F., Farahani, N., Xthona, A., Absar, S.F., Parwani, A., Bui, M., Hartman, D.J.: A practical guide to whole slide imaging: a white paper from the digital pathology association. *Archives of pathology & laboratory medicine* **143**(2), 222–234 (2019)
23. Zhao, Y., Yang, F., Fang, Y., Liu, H., Zhou, N., Zhang, J., Sun, J., Yang, S., Menze, B., Fan, X., et al.: Predicting lymph node metastasis using histopathological images based on multiple instance learning with deep graph convolution. In: *Proceedings of the IEEE/CVF Conference on Computer Vision and Pattern Recognition*. pp. 4837–4846 (2020)
24. Zhou, Z.H., Sun, Y.Y., Li, Y.F.: Multi-instance learning by treating instances as non-iid samples. In: *Proceedings of the 26th annual international conference on machine learning*. pp. 1249–1256 (2009)